Land Surface Temperature and Emissivity Retrieval from Nighttime Middle and Thermal Infrared Images of Chinese Fengyun-3D MERSI-II

Hui Zeng, Huazhong Ren, Jing Nie, Jinshun Zhu, Xin Ye, and Chenchen Jiang

***Abstract*—The second-generation Chinese polar-orbit meteorological satellite Fengyun-3D carries the MEdium-Resolution Spectral Imager (MERSI-II). MERSI-II has 19 solar channels and 6 middle and thermal infrared channels and can provide daily global coverage observation at daytime and nighttime. Land surface temperature (LST) products have a wide range of application requirements. Unfortunately, there is no official LST product of MERSI-II yet. This article proposed a temperature-emissivity separation algorithm to estimate LST and emissivity from two mid-infrared (MIR) and two thermal infrared (TIR) nighttime MERSI-II images. The sensitive analysis and ground validation show the following. First, the algorithm can theoretically retrieve LST with an error of less than 0.7 K, emissivity with errors of about 0.025 for MIR channel and 0.01 for TIR channel, respectively. Second, the nighttime LST retrieval error was approximately 2.19 K, and the bias was approximately 0.60 K among 6 SURFRAD sites and 2 PKULSTNet sites. The retrieved emissivity was cross-validated using MODIS emissivity product over a desert area and its difference was obtained as 0.01 and 0.016 for two TIR channels. Finally, the TES algorithm was applied to obtain LST and emissivity images over North China Plain as an example, and the nighttime LST and land surface emissivity (LSE) were obtained well. As a result, this study shows that the proposed TES algorithm provides an effective way to get LST and LSE image from FY-3D/ MERSI-II nighttime observation, which will improve their applications in different fields.**

***Index Terms*—Fengyun-3D (FY-3D) MEdium-Resolution Spectral Imager (MERSI-II), land surface emissivity (LSE), land surface temperature (LST), mid-infrared (MIR), thermal infrared (TIR).**

I. Introduction

LAND surface temperature (LST) characterizes the thermal radiation information and temporal and spatial changes of the surface under different conditions. As an important basic parameter, it has been widely used in various fields [1], including global climate change, regional evapotranspiration, soil moisture detection, crop yield, urban heat island, forest fire, earthquake prediction and detection, and geological survey [2]–[9].

Owing to the complexity and diversity of the natural surface, LST often changes significantly over time and space. This causes some difficulty for the conventional in-situ measurement of top-soil temperature or air temperature from the meteorological stations to obtain accurate and spatial-continuous LST at a large scale. Fortunately, the development of remote sensing technology, especially thermal infrared (TIR) remote sensing technology and the in-depth research on the mechanism of ground thermal radiation, provides the possibility for long-term LST measurement at global and regional scales.

The retrieval of LST from TIR data observed via remote sensing can be traced back to the 1970s, and it has attracted widespread attention from the scientific community [10]. Up to now, LST has been retrieved successfully from MODerate-resolution Imaging Spectroradiometer (MODIS) [11], Advanced Spaceborne Thermal Emission and Reflectance radiometer (ASTER) [12], Advanced Very High Resolution Radiometer (AVHRR) [13], Thermal Infrared Sensor (TIS) [14] on Landsat 8 and other TIR sensors. The basis and core of remote sensing retrieval of LST are to eliminate surface nonunity emissivity effect and atmospheric effect. Several methods have been proposed to retrieve LST from remote sensing TIR data. For example, the single-window algorithm is suitable for LST retrieval from only one TIR channel observation like Landsat TM/ETM+ [15], but the accuracy of this method is limited by the availability and error of atmospheric parameters. By contrast, multichannel algorithms are commonly used for LST retrieval, among which the split-window (SW) algorithm is the most representative and the most widely used. However, the ground verification results show that the SW algorithm has an overall surface temperature retrieval accuracy between 1 and 2 K under uniform ground and dry atmospheric conditions, and it cannot eliminate the need for pixel emissivity [16].

To eliminate the emissivity effect, a synchronous retrieval algorithm for LST and land surface emissivity (LSE) had been developed. The most common one is the temperature-emissivity separation (TES) algorithm [17]–[20]. The TES algorithm is a physical algorithm that simultaneously obtains LST&LSE from

Manuscript received March 5, 2021; revised May 19, 2021; accepted July 16, 2021. Date of publication July 21, 2021; date of current version August 16, 2021. This work was supported in part by the National Natural Science Foundation of China under Grant 41771369, in part by the National High-Resolution Earth Observation Project of China under Grant 30-H30C01-9004-19/21, in part by the National Key Research and Development Program under Grant 2017YFB0503905-05, and in part by the Open Research Fund of National Earth Observation Data Center under Grant NODAOP2020001. *(Corresponding author: Huazhong Ren.)*

The authors are with the Institute of Remote and Geographic Information System, School of Earth and Space Sciences,Peking University, Beijing 100871, China, with the Key Laboratory of Spatial Information Integration and Its Application, Peking University, Beijing 100871, China, and also with the Geographic Information System Technology Innovation Center, the Ministry of Natural Resources, Beijing 100871, China (e-mail: zenghui@pku.edu.cn; renhuazhong@pku.edu.cn; niejing92@pku.edu.cn; zhujinshun@pku.edu.cn; xinye@pku.edu.cn; jiangchenchen@stu.pku.edu.cn).

Digital Object Identifier 10.1109/JSTARS.2021.3098579

upward thermal radiances measured by the satellite sensor and corresponding atmospheric downward thermal radiance, and has been applied in ASTER [18], [21], MODIS [22], Chinese Gaofen-5 [23], and Sentinel-3 [24]. The TES algorithm does not depend on input emissivity, but it requires multiple TIR or mid-infrared (MIR) data in the atmospheric window and precise atmospheric correction.

MIR data that received thermal radiation information include not only the contribution of surface emission radiation but also the reflected solar thermal radiation during daytime. The two parts are coupled via emissivity; hence, they are difficult to separate. However, at night, MIR data only contain thermal radiation emitted by the surface and have the same radiative transfer equation with TIR data. Therefore, we can use multiple MIR and TIR channels at night to retrieve LST&LSE, to make better use of the MIR channel's radiation information.

The Fengyun-3D (FY-3D) satellite officially only provides LST products based on the microwave imager with a resolution of 25 km. As a sensor similar to MODIS, the MEdium-Resolution Spectral Imager (MERSI-II) has not released an official temperature/emissivity retrieval product. At present, the SW algorithm has been used to retrieve the temperature of MERSI-II data during daytime [25]. However, the SW algorithm cannot work well on nighttime observation because it lacks of visible/near-infrared (VNIR) images to estimate the necessary pixel emissivity. By contrast, the TES algorithm does not require pixel emissivity input and works on both daytime and nighttime observations. However, to date, no research has explored the TES algorithm and verified its availability for MERSI-II image.

Similar to LST products during the day, night LST plays an important role in research on urban heat island, climate change, and crop growth. This study aims to develop an improved TES algorithm to retrieve LST&LSE from MERSI-II MIR and TIR channels images, and use ground measurement data to validate the LST retrieval. If the LSE is assumed unchanged during adjacent several daytime and nighttime observations, the LSE retrieved from nighttime observation can be used in daytime SW algorithm to reduce the dependence of the LST retrieval process on VNIR image and the type of surface coverage.

II. FY-3D/MERSI-II Channel Specification

Launched on November 15, 2017, FY-3D is the fourth satellite in China's second-generation polar-orbiting meteorological satellite family. MERSI-II is one of the important payloads on FY-3D. It has 25 channels with a scanning viewing zenith angle (VZA) range of $\pm 55.4°$ and a ground track repeat cycle of 5.5 days. Its sensor spectral coverage of 0.412–12.0 μm completely covers the channel range of the MERSI-I remote sensors on FY-3A/B/C. Specifically, the satellite has 16 VNIR channels (0.402–0.965 μm), 3 shortwave infrared channels (1.02/1.23–2.155 μm), 2 MIR (3.8 and 4.05 μm), and 4 TIR channels (7.2, 8.55, 10.8, and 12.0 μm). The ground resolution is 1000 m for MIR channels and 250 m for TIR channels. The official provides 250 m and 1000 m resolution level 1 data for TIR channels, and this study uses 1000 m resolution for both MIR and TIR data. In terms of product applications, MERSI-II observations are available at day and night. We can use the similar characteristics of MIR data at night and TIR data of MERSI-II to retrieve LST&LSE.

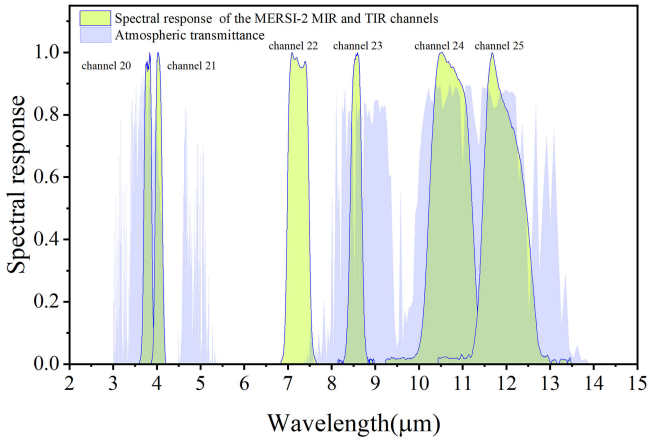

Fig. 1. Atmospheric transmittance and spectral response functions of the MERSI-II MIR and TIR channels.

The spectral filters of the six MIR and TIR channels are shown in Fig. 1. According to the spectral atmospheric transmittance of middle-latitude (mid-lat) summer, channel 22 (7.2 μm) is the water vapor channel with very low transmittance. Thus, this channel is excluded, because its observation mainly contains atmospheric information. Moreover, after checking the accuracy of the radiometric calibration and the corresponding brightness temperatures of the rest of the channels, channel 23 (8.55 μm) is found to suffer from bad calibration. Its brightness temperature was approximately 20 K higher than others; hence, it is also excluded for further analysis. Finally, channels 20 (MIR1), 21 (MIR2), 24 (TIR1), and 25 (TIR2) are chosen to develop the algorithm of retrieving LST & LSE.

III. LST and LSE Retrieval Method Development

A. TES Algorithm

The retrieval of LST is an underdetermined problem. The observation in N channels produces N equations, but they are used to solve $N+1$ unknowns (one LST and N channels' LSE). The TES algorithm adds one equation by establishing an empirical relationship between the minimum emissivity and the maximum-minimum emissivity difference (MMD) of multiple TIR channels, so as to achieve simultaneous retrieval of LST&LSE. The TES algorithm does not rely on the known emissivity of the pixel and can simultaneously retrieve the LST&LSE in the TIR channel. Moreover, the algorithm has high retrieval accuracy for surface types (bare soil, rock, artificial land, etc.) with large differences in emissivity spectra. The RMSE of the emissivity accuracy verification results are generally within 0.015, and the LST accuracy is generally within 1.5 K [18].

At night, MIR and TIR channels have the same radiative transfer process, and the radiance of the top atmosphere measured on the ith channel of the MERSI-II sensor can be expressed as

$$L_i = [\varepsilon_i B_i(T_s) + (1-\varepsilon_i) R_{ai}^{\downarrow}]\tau_i + R_{ai}^{\uparrow} \quad (1)$$

ε_i channel emissivity.
T_s LST.
τ_i atmospheric upward transmittance from the surface to the satellite.
$R_{ai}^{\uparrow}$ atmospheric upward thermal radiance.
$R_{ai}^{\downarrow}$ atmospheric downward thermal radiance.

After the atmospheric correction is completed, the surface-leaving radiance can be obtained

$$L_{s,i} = \varepsilon_i B_i\left(T_s\right) + \left(1-\varepsilon_i\right) R_{ai}^{\downarrow}. \tag{2}$$

Two MIR channels and two TIR channels can obtain four radiation equations (1), but it needs to solve five unknowns (the emissivity of four channels and one LST). The TES algorithm adds an MMD module to solve this ill-posed problem, expressed as

$$\varepsilon_{min} = a + b \cdot \mathrm{MMD}^c. \tag{3}$$

In (3), the MMD represents the difference between the maximum and minimum relative emissivity among participating channels. The MMD made the TES algorithm require at least three channels, which are calculated as

$$\mathrm{MMD} = \max\left(\beta_i\right) - \min\left(\beta_i\right) \tag{4}$$

$$\beta_i = \frac{\varepsilon_i}{\mathrm{mean}\left(\varepsilon\right)}. \tag{5}$$

In (4) and (5), the normalized channel emissivity β_i is the ratio of the emissivity of channel i to the average emissivity of all channels. To obtain coefficients a, b, and c in (3), 74 emissivity spectra were selected from the ASTER emissivity database [26] and the University of California Santa Barbara emissivity database [27], including 28 soil, 19 rock, 14 vegetation, 7 water/snow, and 6 urban surface manmade samples. The spectral response function of the sensor (see Fig. 1) was applied to calculate the channel emissivity of the MERSI-II MIR and TIR channels by using (6)

$$\bar{\varepsilon} = \frac{\int_{\lambda_1}^{\lambda_2} \varepsilon\left(\lambda\right) f\left(\lambda\right) d\lambda}{\int_{\lambda_1}^{\lambda_2} f\left(\lambda\right) d\lambda} \tag{6}$$

where λ_1 and λ_2 are the minimum and maximum wavelengths, respectively, of the current channel; $f(\lambda)$ is the spectral responsivity of the current channel at the wavelength λ and $\varepsilon(\lambda)$ is the emissivity corresponding to wavelength λ.

According to 74 groups of minimum emissivity ($\varepsilon_{\min}$) and the MMD value from (4), coefficients a, b, and c of (3) were regressed as 0.9838, −0.6983, and 0.8038, respectively. The RMSE of $\varepsilon_{\min}$ is recorded as 0.0119, as shown in Fig. 2.

In the normalized emissivity (NEM) module of the TES algorithm, after atmospheric correction, we usually set a maximum initial emissivity value $\varepsilon_{\max} = 0.99$ in all channels to obtain surface temperatures ($T_{\mathrm{s1}}, T_{\mathrm{s2}}, T_{\mathrm{s3}}$, and T_{s4}) from each channel. We then use their maximum temperature $T_{\max}$ as the initial temperature to reverse the initial channels' emissivity ($\varepsilon_1, \varepsilon_2, \varepsilon_3$, and ε_4) of each channel. The standard deviation of the four initial emissivity of these channels is then used as a criterion to determine the next step: if the standard deviation is

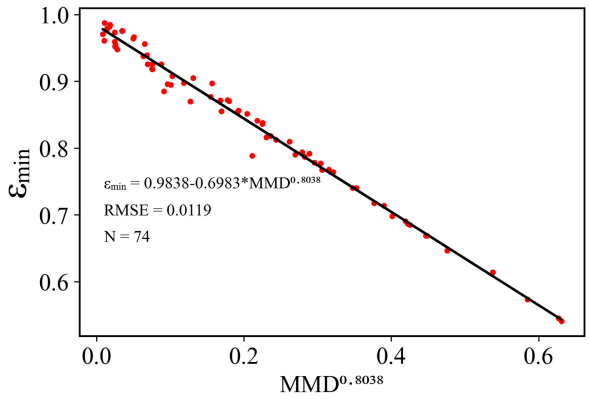

Fig. 2. MMD regression of 74 emissivity spectra.

greater than a threshold of 0.012 (calculated from the rock, soil, and urban surface emissivity in the 74 samples), which indicates that the current surface is probably one of the above land cover, then a new initial maximum emissivity $\varepsilon_{\max}$= 0.971 (average value of the maximum emissivity of the rock, soil, and urban surface samples) will be reinput to the NEM module to update the initial T_s and emissivity. Otherwise, $\varepsilon_{\max}$= 0.984 (average value of the maximum emissivity of vegetation and water samples) will be used instead. On the basis of the initial four channels' emissivity from the NEM module, β_i will be calculated and then used to calculate the value of MMD. After obtaining the value of $\varepsilon_{\min}$ from (3), the emissivity of all channels can be calculated as

$$\varepsilon_i = \varepsilon_{\min} \frac{\beta_i}{\beta_{\min}}. \tag{7}$$

Finally, along with the emissivity, surface-leaving radiance $L_{s,i}$, and the atmospheric downward radiance of four channels, surface temperatures T_{s1}, T_{s2}, T_{s3}, and T_{s4} of each channel will be calculated by using (2). The final LST is captured as the maximum

$$T_s = \max\left(B_i^{-1}\left[\frac{L_{s,i} - \left(1-\varepsilon_i\right) R_{ai}^{\downarrow}}{\varepsilon_i}\right]\right), i = 1, 2, 3, 4. \tag{8}$$

B. Atmospheric Correction for MIR/TIR Channels

The conventional atmospheric correction method based on the radiative transfer models including MODTRAN [28] and RTTOV [29] calculates the atmospheric parameters by inputting the atmospheric profile that matches the space and time of satellite observation. The National Center for Environmental Prediction (NCEP) has provided final operational global analysis (FNL) data to scientific researchers. The currently released data have gradually attracted attention because of its higher temporal and spatial resolution than the reanalysis data. Compared with the global forecast system (GFS) data, FNL data have their own unique advantages. To pursue timeliness, some observations that occurred later than the research period have not been assimilated into GFS data. However, the inclusion of this additional observational data (approximately 10% of the total data volume) makes

the FNL analysis data closer to the true atmospheric state. The NCEP FNL data collect observational data from at least the past 6 h 4 times a day (0:00, 6:00, 12:00, 18:00 UTC) to perform global data analysis. The data include atmospheric parameters such as air pressure, temperature, water vapor content, and ozone ratio with a total of 34 floors (0.4–100 hpa).

The reanalysis data are spatially continuous and have a high temporal resolution. Thus, this article uses the 0.25° × 0.25° NCEP reanalysis data to calculate atmospheric transmittance and the atmospheric upward and downward radiation. The MODTRAN model for atmospheric correction on nighttime MIR and TIR image was used to obtain the surface-leaving radiance and atmospheric downward radiance (2), which are required by the above TES algorithm.

The ground swath of the MERSI-II can reach 2000 km, covering more than 80 grids of the NCEP dataset in the scanning direction. Thus, we divide the entire MERSI-II MIR and TIR images into different windows with a size of 25 km × 25 km (approximately 0.25° × 0.25°). The central longitude and latitude of each window (center point), along with the observation data and time, are then used to extract the atmospheric profiles from the NCEP dataset. All atmospheric profiles are for nighttime over the image area and used to drive MODTRAN to predict the atmospheric parameters (atmospheric upward transmittance, upward thermal radiance, and downward thermal radiance), and then those atmospheric parameters at the center point were interpolated in time and space using linear interpolation method. To reduce the amount of calculation, all pixels in the grid use the same atmospheric data, and the average VZA was used in all pixels in the grid.

IV. Sensitivity Analysis of the TES Algorithm

The retrieval of LST from the TES algorithm can be affected by the system error (caused by MMD empirical regression) of the algorithm itself and other factors in the input data, such as instrument noise, different atmospheric conditions, and different surface types. Therefore, exploring the sensitivity of the algorithm on different atmospheric conditions and different surface land cover types is necessary.

A. Sensitivity Analysis of Different Atmospheric Conditions

To investigate the uncertainty of the different atmospheric conditions of the retrieval results in TES algorithm, three standard atmospheric profiles (i.e., tropical profiles, mid-lat summer, and mid-lat winter) were taken as examples to drive the MODTRAN code to determine the atmospheric parameter of each channel in (1). At the same time, the 74 emissivity samples and different LST levels were used to calculate the surface-leaving radiance. Those LST levels were set as $T_s = T_0 + \Delta T$, where T_0 is the bottom layer air temperature of the atmospheric profiles, whereas ΔT varies from -20 K to 25 K at a step of 5 K [22], [23]. In addition, a 5% Gaussian noise is artificially added to atmospheric parameter $R_{ai}^{\downarrow}$. On the basis of the simulated surface-leaving radiance dataset and noise $R_{ai}^{\downarrow}$, the TES algorithm was then used to obtain the LST&LSE for 1000 random-noise cases.

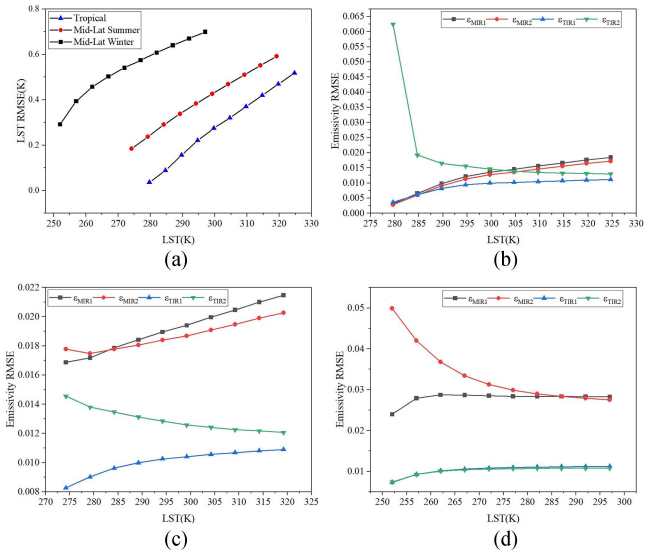

Fig. 3. LST and emissivity retrieval error with a 5% uncertainty in atmospheric parameters of three different atmospheric profiles. (a) LST RMSE. (b) Four channels' emissivity RMSE of the tropical profile. (c) Four channels' emissivity RMSE of mid-lat summer profile. (d) Four channels' emissivity RMSE of mid-lat winter profile.

Fig. 3 shows the RMSE of the retrieved LST&LSE obtained under different T_s for three standard atmospheric conditions. Fig. 3(a) shows that the LST retrieval uncertainty is less than 0.7 K, and increases with the LST value. For the tropical profile [see Fig. 3(b)], when the surface temperature is approximately 280 K, surface emission radiance ($\varepsilon_i B_i(T_s)$) is close to atmospheric downward thermal radiance $R_{ai}^{\downarrow}$, especially in the TIR2 channel. In this case, the land surface and atmospheric environment are like a blackbody, which disables the TES algorithm from separating the temperature and emissivity well. As a result, the emissivity error of this channel is approximately 0.06 near the temperature of 280 K, whereas that of the rest of the channels are relatively smaller in the range of 0.005 and 0.02. For the mid-lat summer profile [see Fig. 3(c)], in most surface temperature cases, the emissivity error of the two MIR channels can reach approximately 0.025. This error value was larger than that of the two TIR channels, which is less than 0.015, especially for high surface temperatures. For the mid-lat winter profile [see Fig. 3(d)], the error of the emissivity of the two MIR channels is more significant by approximately 0.05. On the contrary, the RMSE of emissivity for the two TIR channels is stable, maintaining around 0.01 under varying surface temperature.

B. Sensitivity Analysis of Different Land Cover Types

In order to check the influence of different land cover types on the retrieval error of the TES algorithm, the performance of the TES algorithm on rock, vegetation, soil, water, and manmade samples was analyzed under the tropical, mid-lat summer, and mid-lat winter atmospheric profiles and results are shown in Table I. For the LST retrieval, all error ranges from 0.088 to 0.745K. The rock, vegetation, soil, and water under tropical atmospheric profiles, the manmade under mid-lat atmospheric

TABLE I
SENSITIVITY ANALYSIS OF DIFFERENT LAND CONDITIONS

Sensitivity analysis to different land condition		Rock			Vegetation			Soil			Water			Manmade		
		Tropical	Mid-Lat Summer	Mid-Lat Winter	Tropical	Mid-Lat Summer	Mid-Lat Winter	Tropical	Mid-Lat Summer	Mid-Lat Winter	Tropical	Mid-Lat Summer	Mid-Lat Winter	Tropical	Mid-Lat Summer	Mid-Lat Winter
LST	*RMSE(K)*	0.187	0.265	0.448	0.332	0.471	0.745	0.088	0.114	0.175	0.034	0.057	0.127	0.248	0.240	0.259
	ΔMax	0.395	0.355	0.055	0.165	0.695	0.875	0.215	0.275	0.405	0.075	0.095	0.105	0.285	0.125	0.035
	ΔMin	-0.895	-0.895	-1.345	-1.015	-1.835	-2.825	-0.315	-0.365	-0.445	-0.075	-0.135	-0.345	-0.725	-0.705	-0.635
ε_{MIR1}	*RMSE*	0.008	0.012	0.023	0.015	0.022	0.039	0.004	0.005	0.008	0.002	0.003	0.007	0.011	0.012	0.014
	ΔMax	0.033	0.033	0.068	0.040	0.064	0.136	0.015	0.013	0.023	0.003	0.005	0.030	0.029	0.028	0.029
	ΔMin	-0.014	-0.015	-0.002	-0.013	-0.028	-0.044	-0.007	-0.009	-0.015	-0.003	-0.004	-0.007	-0.013	-0.009	-0.001
ε_{MIR2}	*RMSE*	0.007	0.012	0.029	0.014	0.021	0.047	0.003	0.005	0.011	0.001	0.003	0.011	0.011	0.012	0.016
	ΔMax	0.031	0.032	0.104	0.036	0.058	0.178	0.013	0.013	0.047	0.003	0.005	0.067	0.027	0.030	0.035
	ΔMin	-0.013	-0.014	-0.002	-0.012	-0.030	-0.087	-0.006	-0.008	-0.030	-0.003	-0.004	-0.014	-0.012	-0.009	-0.001
ε_{TIR1}	*RMSE*	0.005	0.006	0.008	0.010	0.011	0.014	0.003	0.003	0.003	0.001	0.001	0.003	0.008	0.006	0.005
	ΔMax	0.018	0.016	0.021	0.040	0.033	0.048	0.016	0.007	0.007	0.004	0.003	0.009	0.021	0.013	0.010
	ΔMin	-0.010	-0.008	-0.001	-0.012	-0.014	-0.014	-0.005	-0.005	-0.007	-0.002	-0.002	-0.002	-0.009	-0.004	-0.001
ε_{TIR2}	*RMSE*	0.010	0.008	0.008	0.043	0.014	0.014	0.025	0.004	0.003	0.011	0.002	0.003	0.032	0.008	0.005
	ΔMax	0.022	0.022	0.021	0.053	0.037	0.047	0.021	0.012	0.007	0.032	0.004	0.009	0.038	0.023	0.010
	ΔMin	-0.083	-0.011	-0.001	-0.439	-0.023	-0.014	-0.241	-0.006	-0.006	-0.069	-0.003	-0.002	-0.219	-0.007	-0.001

TABLE II
DETAILED INFORMATION AND VALIDATION RESULTS OF EACH GROUND SITE

Site Names	Program	Latitude	Longitude	Land Cover	Image Number	RMSE (K)	Bias (K)
Bondville_IL (BON)	SURFRAD	40.05°N	88.37°W	Cropland	27	1.54	0.29
Goodwin_Creek_MS (GWN)	SURFRAD	34.25°N	89.87°W	Pasture	32	2.48	2.15
Penn_State_PA (PSU)	SURFRAD	40.72°N	77.93°W	Cropland	20	2.2	1.47
Sioux_Falls_SD (SXF)	SURFRAD	43.73°N	96.62°W	Cropland	28	1.91	–0.69
Fort_Peck_MT (FPK)	SURFRAD	48.31°N	105.10°W	Grassland	17	1.83	0.29
Boulder_CO (TBL)	SURFRAD	40.12°N	105.24°W	Grassland	18	2.22	−1.63
Hebei_Chengde (HBC)	PKULSTNet	42.41°N	117.25°E	Grassland	27	2.14	0.96
Henan_Hebi (HNH)	PKULSTNet	35.72°N	114.32°E	Cropland	25	2.86	1.12
Total RMSE: 2.19 K, total bias: 0.60 K							

profiles have the lowest RMSE. The vegetation and water have similar LST retrieval error level, which is about 2–4 times larger in mid-lat winter than that in tropical. As for the emissivity retrieval, the retrieval error of emissivity in TIR channels (avg_TIR1:0.006 and avg_TIR2:0.013)) is generally lower than in MIR channels (avg_MIR1: 0.012 and avg_MIR2:0.014). This error is similar with that of the ASTER emissivity [30]. Soil and water have better performance than other land types. It is also found that all land cover types in emissivity retrieval under tropical atmospheric profiles have a much bigger min error than other kinds of atmospheric profiles. The vegetation has a larger error of emissivity in MIR2 channels, especially under mid-lat winter profiles, the RMSE is up to 0.047.

V. VALIDATION AND APPLICATION

A. Validation of LST Using Ground-Measured Dataset

To validate the retrieval results and evaluate the accuracy of the algorithm, the ground-measured surface temperature was calculated according to the ground radiation measurement results and used as the reference true value of the LST for comparison. In this article, six sites under the Surface Radiation Budget Network (SURFRAD) program [31], [32] in the USA, and two sites under the Peking University LST Network (PKULSTNet) in China [16] were used to validate the results. Table II shows the information about these sites.

1) Surface Radiation Budget Network: The surface measurement data of SURFRAD sites provided the surface upward and atmospheric downward thermal radiation in the wavelength range of 3–50 μm, in an interval of 3 minutes (before January 2009)/1 min (after January 2009). SURFRAD sites use pyrgeometers for measuring thermal radiance, which with a measurement error range of 3–5 W/m², corresponding to an error range of surface temperature of 0.5–0.8 K [31]. According to the near-surface radiative transfer equation (the atmospheric transmittance is approximately 1.0 and the atmospheric upward radiation is approximately 0.0) and the Stefan–Boltzmann law, the reference surface temperature measured on the ground can be calculated as follows:

$$T_{\text{ground}} = \left[\frac{L^{\uparrow} - (1-\bar{\varepsilon})R^{\downarrow}}{\bar{\varepsilon}\sigma}\right]^{\frac{1}{4}} \tag{9}$$

σ Stefan–Boltzmann constant ($5.67 \times 10^{-8}\text{W}\cdot\text{m}^{-2}\cdot\text{K}^{-4}$).
$\bar{\varepsilon}$ ground broadband emissivity (BBE).
$L^{\uparrow}$ surface upward TIR irradiance.
$R^{\downarrow}$ atmospheric downward TIR irradiance.

The ground BBE is obtained from MODIS emissivity product (MYD21A1N) by using the following equation [33]:

$$\bar{\varepsilon} = 0.095 + 0.329 \times \varepsilon_{29} + 0.572 \times \varepsilon_{31}. \tag{10}$$

2) Peking University LST Network: Unlike the SURFRAD sites, the two radiometers of PKULSTNet sites called SI-411 from Apogee Instruments Company are used to measure the surface-leaving brightness temperature T_1 and the atmosphere downward brightness temperature T_2 from a 2-m tower [16], [24], [34]. Its radiometers are sensitive to the wavelength of 8 μm to 14 μm. The integral of Planck's law over a wavelength

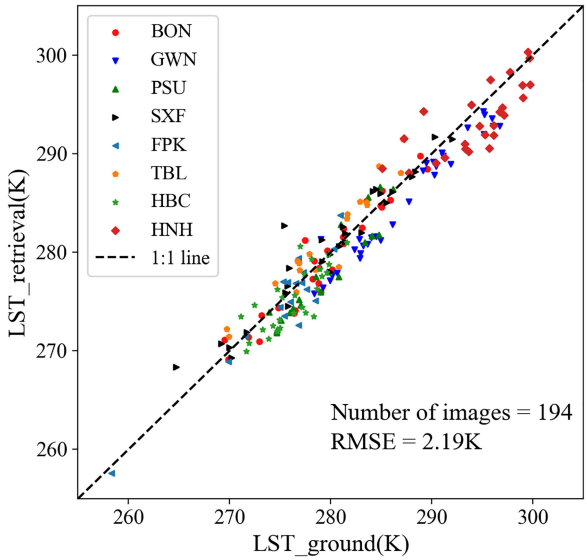

Fig. 4. Comparison between MERSI-II LST and ground LST over different ground sites.

of 8 μm to 14 μm can be defined as:

$$M = \sigma' T^4 \tag{11}$$

M total irradiance over 8–14 μm.

σ' a constant, but not equal to the Stefan–Boltzmann constant.

Thus, T_{ground} can be calculated as [16]:

$$T_{\text{ground}} = \left[\frac{\sigma' T_1^4 - (1-\bar{\varepsilon})\sigma' T_2^4}{\bar{\varepsilon}\sigma'}\right]^{\frac{1}{4}} = \left[\frac{T_1^4 - (1-\bar{\varepsilon})T_2^4}{\bar{\varepsilon}}\right]^{\frac{1}{4}}. \tag{12}$$

Equation (12) shows that the calculation of T_{ground} is independent of the value of σ', it will not be influenced by using a spectral wavelength from 8 to 14 μm. On these eight sites, 194 clear-sky nighttime MERSI-II images were collected in years 2019 and 2020. Their LSTs were retrieved by using the above proposed TES algorithms. At the same time, the corresponding ground measurement LST is calculated according to (9) and (12) for comparison. Since the ground temperature may have some abrupt errors due to the local meteorological environment change (such as wind and cloud shadow), the average ground temperature measured within 10 min before and after the satellite observation is used as the reference ground temperature (T_{ground}). However, if the standard deviation of those ground-measured temperatures in the 10 min was greater than 1 K, the corresponding T_{ground} would be discarded. Fig. 4 shows the scatter diagrams between satellite-retrieved LST (denoted as LST_retrieval) and the temperature of the ground site (denoted as LST_ground). Most points are along the 1:1 line. For the TES algorithm, the RMSE is 2.19 K and the temperature bias is 0.60 K. These results indicated the following. 1) The RMSEs of sites Bondville_IL (BON), Sioux_Falls_SD (SXF), and Fort_Peck_MT (FPK) are less than 2.0 K, while Goodwin Creek_MS (GWN), Penn_State_PA (PSU), Boulder_CO (TBL), Hebei_Chengde (HBC), and Henan_Hebi (HNH) have values greater than 2.0 K (see Table II). 2) The smallest error was obtained at BON (RMSE = 1.54 K, bias = 0.29 K), and the largest error was observed at the HNH site (RMSE = 2.86 K, bias = 1.12 K). Generally, based on current validation results, the temperature error generated by the proposed TES algorithm for nighttime MERSI-II images may be in the range of 1.0–2.5 K.

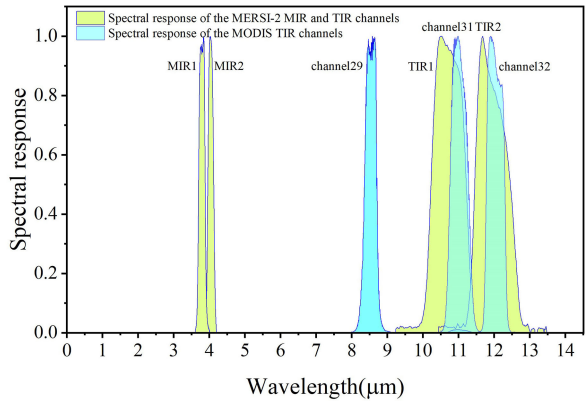

Fig. 5. Spectral response functions of the MERSI-II and MODIS channels.

B. Cross-Validation of Emissivity Using MODIS Product

A TES algorithm was proposed to dynamically retrieve both LST and channel emissivity simultaneously from the MODIS TIR channels 29, 31, and 32 [35] and then used to generate MODIS new daily emissivity product (MYD21A1N) at 1 km pixel size. This kind of MODIS emissivity provides an opportunity to crossly validate the emissivity from MERSI-II. As shown in Fig. 5, we found that the spectral response functions of the two MERSI-II TIR channels are similar to the MODIS TIR channels. The following relationship is obtained by fitting the 74 emissivity samples, causing R^2 and RMSE are (0.96, 0.005) and (0.97, 0.002) for the two TIR channels, respectively

$$\varepsilon_{TIR1} = 1.0723 \times \varepsilon_{31} - 0.071064 \tag{13}$$

$$\varepsilon_{TIR2} = 0.9782 \times \varepsilon_{32} + 0.020426. \tag{14}$$

Two typical surfaces in the Taklimakan Desert (the largest desert in China)—desert and vegetation were chosen for cross-validation of emissivity. As shown in Fig. 6, nighttime images of MERSI-II, which were observed at 20:50UTC (4:50 local time) on July 27, 2019 was selected, and their corresponding LST and LSE were retrieved using the proposed TES algorithm. Meanwhile, MODIS emissivity daily product with the same day were collected. Fig. 6(a) shows the comparison of the emissivity of MERSI-II TIR1 and MODIS channel 31 over the desert area. The upper part is the MERSI-II image, the lower part is the MODIS image, and the right is the distribution histogram of the emissivity difference between the two channels. Fig. 6(b) shows the comparison of the emissivity results of MERSI-II TIR2 and MODIS channel 32 in the desert area. As the same, Fig. 6(c)

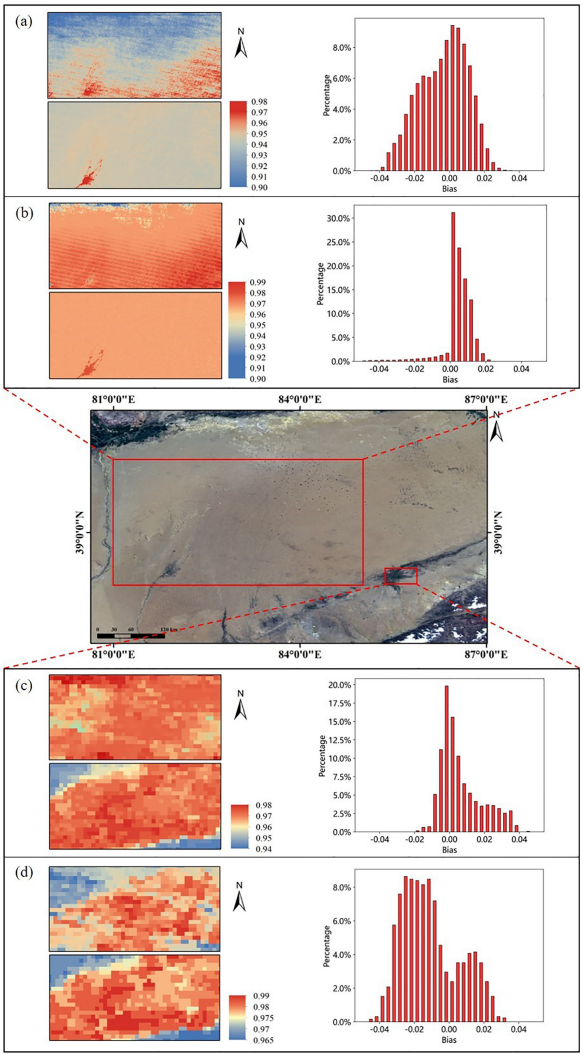

Fig. 6. Comparison of the emissivity of MERSI-II TIR channels and MODIS TIR channels.

and (d) shows the comparison of the emissivity retrieval results of MERSI-II and MODIS over the vegetation area.

In the desert area, the average bias of the MERSI-II TIR1 channel emissivity and the MODIS channel31 emissivity was −0.0048, and the RMSE of the difference was 0.016. The average bias of the TIR2 channel emissivity and the MODIS channel32 emissivity was 0.0045, and the RMSE of the difference was 0.010. In Fig. 6(b), it can be found that in the MERSI-II emissivity image, there are obvious regular noise strips in the area below the image, which leads to the distribution of the emissivity difference histogram mainly on the right.

In the vegetation area, the average bias of MERSI-II TIR1 channel emissivity and the MODIS channel 31 emissivity was 0.0075, and the RMSE of the difference was 0.014. The average bias of MERSI-II TIR2 channel emissivity and the MODIS channel 32 emissivity was −0.011, and the RMSE of the difference was 0.019.

From the above result, it was found that over the two uniform land covers areas, the emissivity of the MERSI-II image is relatively consistent with the MODIS emissivity product. However, it was also found because of a relatively higher noise level, the MERSI-II emissivity image retrieval does not show as smooth as MODIS image.

C. Applications of LST and Emissivity Retrieval

Two nighttime images of MERSI-II were collected for retrieval application, and they were selected with the least cloud coverage based on MERSI-II cloud mask label dataset. The two images were observed at 18:30 and 18:35 UTC (02:30 and 02:35 local time) on September 25, 2019, to validate the application of the above TES algorithm. The two images were merged and clipped according to the study area boundary. The study area is in the North China Plain, within 31.3°–42.6° latitude and 110.2°–122.8° longitude. As shown in Fig. 7(a), the nighttime LST ranges from 262 K to 312 K but mainly within 280–295 K [see Fig. 7(b)]. The urban region had a larger LST value than the rural region. The northwest part of this area is a mountainous region with a low surface temperature, while the middle part is a large plain, mainly covering farmland and urban areas, so the surface temperature is relatively high. In the east coast area, the temperature was higher at night. The emissivity images shown in Fig. 7(c)–(f) can usually represent the spatial pattern of the study area. According to the emissivity histograms in Fig. 7(g), the emissivity of the MIR channel is usually smaller (0.76–1.0) than the emissivity of the two TIR channels (0.90–1.0). For most pixels, the order of channel emissivity is as follows: MIR2 $<$MIR1 $<$ TIR2 $<$ TIR1.

VI. Discussions and Conclusion

For nighttime observations without solar radiance, MIR (3–5 μm) and TIR emission of the land surface have the same radiative transfer process. The MIR data with higher atmospheric transmittance and lower sensitivity to LSE, FY-3D/MERSI-II sensor provides data with rich frequency channels. Hence, we choose two MIR and two TIR channels of nighttime MERSI-II observations and developed a four-channel TES algorithm to estimate LST and channel emissivity from MERSI-II, to make full use of the spectral information and improve the retrieval accuracy. According to the sensitivity analysis, even with a 5% uncertainty in atmospheric correction, the TES algorithm can theoretically retrieve LST&LSE with errors less than 0.7 K and 0.025. In terms of emissivity retrieval, TIR channels have higher accuracy than MIR channels. The ground measurement LST datasets from the six sites of the SURFRAD program and two sites of the PKULSTNet program were used to validate the retrieved LST from nighttime MERSI-II images, the result shows that the LST RMSE is about 2.19 K, and the LST bias is approximately 0.6 K. The TIR channel emissivity were cross-validated with MODIS emissivity product over desert and vegetation coverage surface. As for desert surface, the emissivity bias was 0.0048 and 0.0045 while the emissivity RMSE was 0.016 and 0.010 for the MERSI-II TIR1 and TIR2 emissivity, respectively. Over the vegetation surface, the above bias was 0.0075 and −0.011 and the RMSE was 0.014 and 0.019, respectively. Finally, the new four-channel TES algorithm was used to

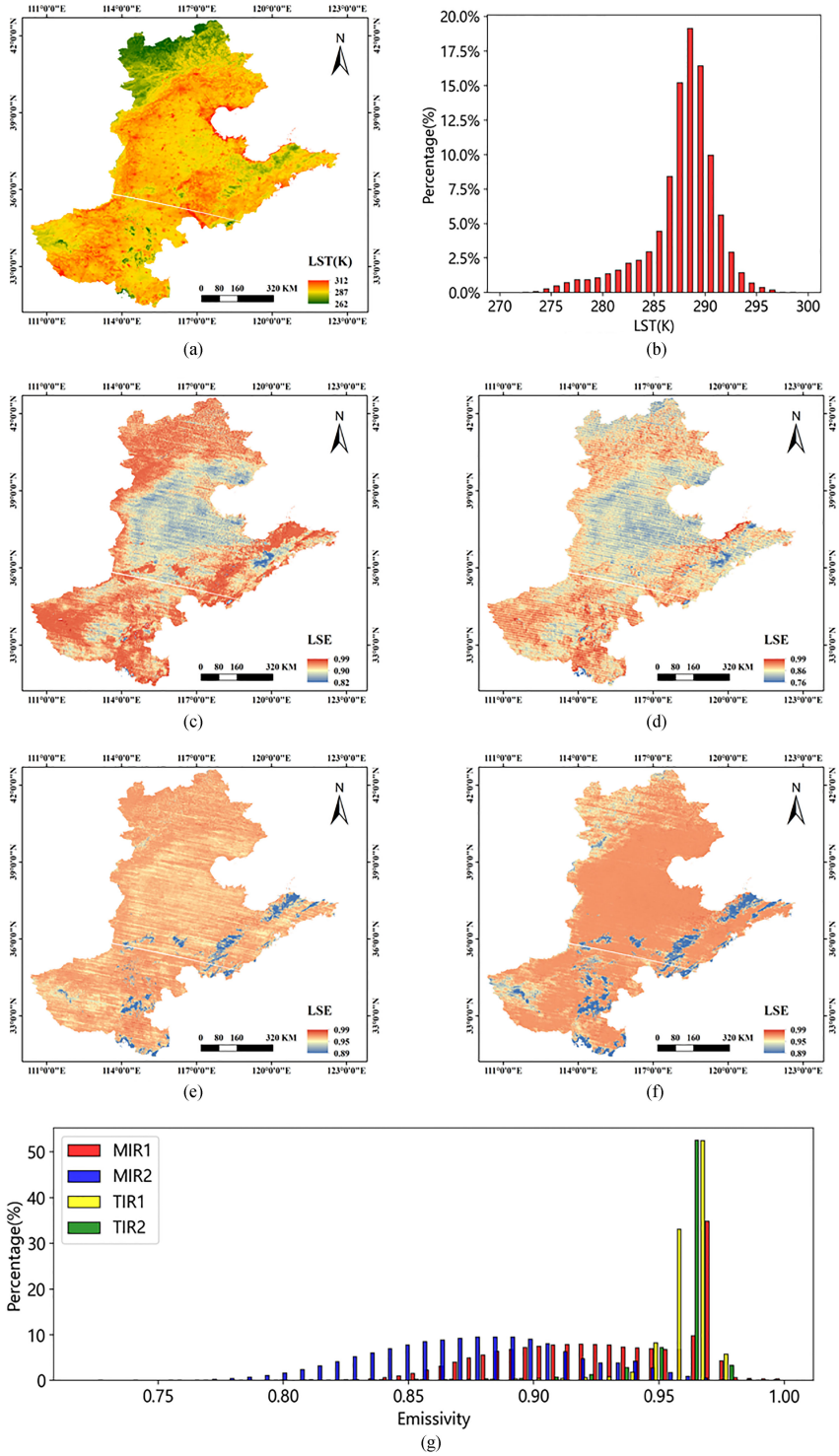

Fig. 7. Application of LST and emissivity retrieval from nighttime FY-3D/MERSI-II observation on September 25, 2019, over North China Plain. (a) Nighttime LST. (b) LST histogram. (c) MIR1 channel emissivity. (d) MIR2 channel emissivity. (e) TIR1 channel emissivity. (f) TIR2 channel emissivity. (g) Four-channel emissivity histogram.

retrieve LST and emissivity images over the North China Plain and got reasonable retrieval results.

However, it was found that under some tropical atmospheric profiles, the atmospheric downward radiance of the second TIR channel was very closed to or even larger than ground emission radiance at around 280 K, which made the system of land surface and atmosphere act as a blackbody-like system and finally caused the TES algorithm to have significant uncertainty in separating temperature and emissivity. In this case, this study will use the rest three channels in the TES algorithm to improve the accuracy. Although 194 images over 8 ground sites were used for nighttime LST validation, the land cover

is mainly cropland and grassland. The scale effect between ground-based point LST and pixel LST can possibly cause some uncertainty in the current validation technique. Therefore, the ground validation of the LST and emissivity over different land cover and atmospheric conditions are required in the near future. Besides, some regular noise strips were found in the emissivity images. These noise strips may be caused by the push-broom scanning manner of the MERSI-II and incomplete radiometric calibration between different detectors. The MERSI-II sensor can be calibrated using on-board blackbody instrument or using ground and cross-calibration methods to check the dynamic stability of the calibration and improve the calibration accuracy.

This article did not need VNIR image to estimate pixel emissivity but uses the physical TES algorithm to obtain LST&LSE from nighttime observation. If the LSE was assumed unchanged in a short period, the obtained LSE can be also used in the SW algorithm for LST retrieval from the adjacent daytime image. Moreover, the TES algorithm is promising to provide global LST&LSE product from MERSI-II images, as done from the MODIS [22] and ASTER [36] product programs. According to the current literature, the LST products can be used in fire detection, farmland drought monitoring, and other applications, while LSE products can be used for mineral identification, and energy balance estimation [2]–[9]. The residual error caused by an incorrect atmospheric correction in the TES algorithm causes great uncertainty in the obtained LST&LSE. In addition, the traditional atmospheric correction algorithm has a large error when the water vapor content is high, and this uncertainty will lead to a larger LST&LSE retrieval error [37], [38]. Tonooka first proposed water vapor scaling (WVS) atmospheric correction method. A water-vapor profile in global assimilated data is believed not to be always accurate; hence, it may cause a significant error to the single-channel algorithm. Nonetheless, this error may be reduced by an appropriate scaling of a water-vapor profile [39]. According to the original WVS algorithm, the whole algorithm processing involves the following steps. First, two water vapor factor values (e.g., 1 and 0.7) for each atmospheric grid were used to run MODTRAN to obtain two sets of transmittance and atmospheric upward radiation values. Second, the EMC/WVD algorithm, the Pierluissi band model, and coefficients (WVS regression coefficients, band model parameters, and atmospheric downward radiation regression coefficients simulated by atmospheric profile libraries) were applied to obtain the water vapor factor values of each gray volume pixel. Finally, a new updated value of atmospheric parameters from the WVS factor is obtained. Actually, this article tried to use the WVS method. However, when the VZA is greater than 45°, the RMSE of the WVS regression coefficients fitted to the MERSI-II channels using night Seebor V5.1 profile data [40] was greater than 2.0 K, which is too large to guarantee the accuracy of subsequent calculations. As a result, the WVS method was not used in the present study.

Acknowledgment

The FengYun-3 images were downloaded from the National Satellite Meteorological Center of China Meteorological Administration; the NCEP profile was downloaded from Global Forecast System. The SURFRAD data were from Earth System Research Laboratory Global Monitoring Division, and the PKULSTNet data were collected by the authors.

References

[1] Z.-L. Li *et al.*, "Satellite-derived land surface temperature: Current status and perspectives," *Remote Sens. Environ.*, vol. 131, pp. 14–37, Apr. 2013.

[2] A. J. Arnfield, "Two decades of urban climate research: A review of turbulence, exchanges of energy and water, and the urban heat island," *Int. J. Climatol.,* vol. 23, no. 1, pp. 1–26, Jan. 2003, doi: 10.1002/joc.859.

[3] W. M. Bastiaanssen, M. Menenti, R. Feddes, and A. Holtslag, "A remote sensing surface energy balance algorithm for land (SEBAL) - 1. Formulation," *J. Hydrol.,* vol. 212, no. 1-4, pp. 198–212, Dec. 1998, doi: 10.1016/S0022-1694(98)00253-4.

[4] J. Kalma, T. R. McVicar, and M. F. McCabe, "Estimating land surface evaporation: A review of methods using remotely sensed surface temperature data," *Surv. Geophys.,* vol. 29, no. 4/5, pp. 421–469, Oct. 2008, doi: 10.1007/s10712-008-9037-z.

[5] F. Kogan, "Operational space technology for global vegetation assessment," *Bull. Amer. Meteorol. Soc.,* vol. 82, no. 9, pp. 1949–1964, Sep. 2001, doi: 10.1175/1520-0477(2001)082<1949:Ostfgv>2.3.Co;2.

[6] Z. Su, "The surface energy balance system (SEBS) for estimation of turbulent heat fluxes," *Hydrol. Earth Syst. Sci.,* vol. 6, no. 1, pp. 85–99, Feb. 2002, doi: 10.5194/hess-6-85-2002.

[7] J. Voogt and T. Oke, "Thermal remote sensing of urban climates," *Remote Sens. Environ.,* vol. 86, no. 3, pp. 370–384, Aug. 15, 2003, doi: 10.1016/S0034-4257(03)00079-8.

[8] Q. Weng, "Thermal infrared remote sensing for urban climate and environmental studies: Methods, applications, and trends," *ISPRS J. Photogramm. Remote Sens.,* vol. 64, no. 4, pp. 335–344, Jul. 2009, doi: 10.1016/j.isprsjprs.2009.03.007.

[9] Q. Weng, D. Lu, and J. Schubring, "Estimation of land surface temperature-vegetation abundance relationship for urban heat island studies," *Remote Sens. Environ.,* vol. 89, no. 4, pp. 467–483, Feb. 29, 2004, doi: 10.1016/j.rse.2003.11.005.

[10] McMillin and M. Larry, "Estimation of sea surface temperatures from two infrared window measurements with different absorption," *J. Geophys. Res.,* vol. 80, no. 36, pp. 5113–5117, 1975.

[11] M. Neteler, "Estimating daily land surface temperatures in mountainous environments by reconstructed MODIS LST data," *Remote Sens.,* vol. 2, no. 1, pp. 333–351, 2010.

[12] J. Jiménez-Muñoz and J. Sobrino, "A single-channel algorithm for land-surface temperature retrieval from ASTER data," *IEEE Geosci. Remote Sci. Lett.,* vol. 7, no. 1, pp. 176–179, Jan. 2010.

[13] A. Pinheiro, J. Privette, R. Mahoney, and C. Tucker, "Directional effects in a daily AVHRR land surface temperature dataset over Africa," *IEEE Trans. Geosci. Remote Sens.,* vol. 42, no. 9, pp. 1941–1954, Sep. 2004.

[14] O. Rozenstein, Z. Qin, Y. Derimian, and A. Karnieli, "Derivation of land surface temperature for landsat-8 TIRS using a split window algorithm," *Sensors,* vol. 14, no. 4, pp. 5768–5780, 2014.

[15] Z. Qin, A. Karnieli, and P. Berliner, "A mono-window algorithm for retrieving land surface temperature from landsat TM data and its application to the Israel-Egypt border region," *Int. J. Remote Sens.,* vol. 22, no. 18, pp. 3719–3746, Dec. 2001, doi: 10.1080/01431160010006971.

[16] Y. Zheng *et al.*, "Land surface temperature retrieval from sentinel-3a sea and land surface temperature radiometer, using a split-window algorithm," *Remote Sens.,* vol. 11, no. 6, Mar. 17, 2019, Art no. 650, doi: 10.3390/rs11060650.

[17] B. Carli *et al.*, "First results of MIPAS/ENVISAT with operational level 2 code," *Adv. Space Res.,* vol. 33, no. 7, pp. 1012–1019, 2004, doi: 10.1016/S0273-1177(03)00584-2.

[18] A. Gillespie, S. Rokugawa, T. Matsunaga, J. S. Cothern, S. Hook, and A. B. Kahle, "A temperature and emissivity separation algorithm for advanced spaceborne thermal emission and reflection radiometer (ASTER) images," *IEEE Trans. Geosci. Remote Sens.,* vol. 36, no. 4, pp. 1113–1126, Jul. 1998, doi: 10.1109/36.700995.

[19] N. Malakar and G. Hulley, "A water vapor scaling model for improved land surface temperature and emissivity separation of MODIS thermal infrared data," *Remote Sens. Environ.,* vol. 182, pp. 252–264, Sep. 1, 2016, doi: 10.1016/j.rse.2016.04.023.

[20] T. Schmugge, A. French, J. Ritchie, A. Rango, and H. Pelgrum, "Temperature and emissivity separation from multispectral thermal infrared observations," *Remote Sens. Environ.,* vol. 79, no. 2/3, pp. 189–198, Feb. 2002, doi: 10.1016/S0034-4257(01)00272-3.

[21] D. Sabol, A. Gillespie, E. Abbott, and G. Yamada, "Field validation of the ASTER temperature-emissivity separation algorithm," *Remote Sens. Environ.,* vol. 113, no. 11, pp. 2328–2344, Nov. 16, 2009, doi: 10.1016/j.rse.2009.06.008.

[22] G. Hulley and S. Hook, "Generating consistent land surface temperature and emissivity products between ASTER and MODIS data for earth science research," *IEEE Trans. Geosci. Remote Sens.,* vol. 49, no. 4, pp. 1304–1315, Apr. 2011, doi: 10.1109/Tgrs.2010.2063034.

[23] H. Ren, X. Ye, R. Liu, J. Dong, and Q. Qin, "Improving land surface temperature and emissivity retrieval from the Chinese Gaofen-5 satellite using a hybrid algorithm," *IEEE Trans. Geosci. Remote Sens.,* vol. 56, no. 2, pp. 1080–1090, Feb. 2018, doi: 10.1109/TGRS.2017.2758804.

[24] J. Nie, H. Ren, Y. Zheng, D. Ghent, and K. Tansey, "Land surface temperature and emissivity retrieval from nighttime middle-infrared and thermal-infrared sentinel-3 images," *IEEE Geosci. Remote Sens. Lett.,* vol. 18, no. 5, pp. 915–919, May 2021, doi: 10.1109/lgrs.2020.2986326.

[25] H. Wang *et al.*, "A split window algorithm for retrieving land surface temperature from FY-3D MERSI-II data," *Remote Sens.,* vol. 11, no. 18, pp. 2083, Sep. 2019, doi: 10.3390/rs11182083.

[26] D. Ghent, G. Corlett, F. Gottsche, and J. Remedios, "Global land surface temperature from the along-track scanning radiometers," *J. Geophysical Res.: Atmospheres,* vol. 122, no. 22, pp. 12167–12193, Nov. 27, 2017, doi: 10.1002/2017jd027161.

[27] A. Baldridge, S. Hook, C. Grove, and G. Rivera, "The ASTER spectral library version 2.0," *Remote Sens. Environ.,* vol. 113, no. 4, pp. 711–715, Apr. 15, 2009, doi: 10.1016/j.rse.2008.11.007.

[28] L. Abreu and G. Anderson, "The MODTRAN 2/3 report and LOWTRAN 7 model,", 1996, Contract F19628-91-C-0132.

[29] R. Saunders *et al.*, "An update on the RTTOV fast radiative transfer model (currently at version 12)," *Geosci. Model Develop.*, vol. 11, no. 7, pp. 2717–2737, 2018.

[30] D. E. Sabol, A. R. Gillespie, E. Abbott, G. Yamada, "Field validation of the ASTER temperature-emissivity separation algorithm," *Remote Sens. Environ.,* vol. 113, no. 11, pp. 2328–2344, 2009, doi: 10.1016/j.rse.2009.06.008.

[31] J. Augustine, G. Hodges, C. Cornwall, J. Michalsky, and C. Medina, "An update on SURFRAD-The GCOS surface radiation budget network for the continental united states," *J. Atmos. Ocean. Technol.,* vol. 22, no. 10, pp. 1460–1472, Oct. 2005, doi: 10.1175/Jtech1806.1.

[32] K. Wang and S. Liang, "Evaluation of ASTER and MODIS land surface temperature and emissivity products using long-term surface longwave radiation observations at SURFRAD sites," *Remote Sens. Environ.,* vol. 113, no. 7, pp. 1556–1565, Jul. 15, 2009, doi: 10.1016/j.rse.2009.03.009.

[33] J. Cheng, S. Liang, Y. Yao, and X. Zhang, "Estimating the optimal broadband emissivity spectral range for calculating surface longwave net radiation," *IEEE Geosci. Remote Sens. Lett.,* vol. 10, no. 2, pp. 401–405, Mar. 2013.

[34] X. Ye *et al.*, "Cross-calibration of chinese gaofen-5 thermal infrared images and its improvement on land surface temperature retrieval," *Int. J. Appl. Earth Observ. Geoinf.*, vol. 101, 2021, Art. no. 102357, doi: 10.1016/j.jag.2021.102357.

[35] G. Hulley and S. Hook, "MOD21A2 MODIS/Terra land surface temperature/3-band emissivity 8-Day L3 global 1km SIN grid V006 [Data set]," in NASA EOSDIS Land Processes DAAC, 2017.

[36] G. Hulley, S. Hook, E. Abbott, N. Malakar, T. Islam, and M. Abrams, "The ASTER global emissivity dataset (ASTER GED): Mapping earth's emissivity at 100 meter spatial scale," *Geophys. Res. Lett.,* vol. 42, no. 19, pp. 7966–7976, Oct. 16, 2015, doi: 10.1002/2015gl065564.

[37] A. Gillespie, E. Abbott, L. Gilson, G. Hulley, J. Jiménez-Muñoz, and J. Sobrino, "Residual errors in ASTER temperature and emissivity standard products AST08 and AST05," *Remote Sens. Environ.,* vol. 115, no. 12, pp. 3681–3694, 2011.

[38] G. Hulley, C. Hughes, and S. Hook, "Quantifying uncertainties in land surface temperature and emissivity retrievals from ASTER and MODIS thermal infrared data," *J. Geophys. Res., Atmos.riu,* vol. 117, no. D23, 2012, doi: 10.1029/2012JD018506.

[39] H. Tonooka, "An atmospheric correction algorithm for thermal infrared multispectral data over land-a water-vapor scaling method," *IEEE Trans. Geosci. Remote Sens.,* vol. 39, no. 3, pp. 682–692, Mar. 2001.

[40] S. W. Seemann, E. Borbas, R. Knuteson, G. Stephenson, H.-L. Huang, "Development of a global infrared land surface emissivity database for application to clear sky sounding retrievals from multispectral satellite radiance measurements," *J. Appl. Meteorol. Climatol.*, vol. 47, no. 1, pp. 108–123, 2008.

Hui Zeng received the B.S. degree in geographic information system from Lanzhou Jiaotong University, Lanzhou, China, in 2011. He is currently working toward the master's degree in cartography and geographic information system with the Institute of Remote and Geographic Information System, School of Earth and Space Sciences, Peking University, Beijing, China.

His main research interests include land surface temperature/emissivity estimate from thermal infrared image.

Huazhong Ren received the Ph.D. degree in cartography and geographic information system from Beijing Normal University, Beijing, China, and from Université de Strasbourg, Strasbourg, France, in 2013.

Since 2016, he is an Assistant Professor with the Institute of Remote Sensing and Geographic Information System, School of Earth and Space Sciences, Peking University, Beijing, China. His research interests include land surface temperature/emissivity estimate from thermal infrared remote sensing data.

Jing Nie received the master's degree in cartography and geographic information system from the Institute of Remote Sensing and Geographic Information System, School of Earth and Space Sciences, Peking University, Beijing, China, in 2021.

Her research interests include land surface temperature/emissivity estimate from hyperspectral thermal infrared image.

Jinshun Zhu received the B.S. degree in cartography and geographic information system, in 2019, from Peking University, Beijing, China, where he is currently working toward the Ph.D. degree with the Institute of Remote Sensing and Geographic Information System, School of Earth and Space Sciences.

His research interests mainly concentrate on middle infrared and thermal infrared remote sensing.

Xin Ye received the B.S. degree in computer science and technology from Beijing Normal University, Beijing, China, in 2012, and the Ph.D. degree in cartography and geographic information system from Peking University, Beijing, China, in 2017.

He is currently a Postdoctoral Researcher with the Institute of Remote Sensing and Geographic Information System, School of Earth and Space Sciences, Peking University. His research interests mainly concentrate on thermal infrared remote sensing and deep-learning in remote sensing.

Chenchen Jiang received the B.S. degree from People's Public Security University of China, Beijing, China, in 2020 and the master's degree of computer networks and security. She is currently working toward the Ph.D. degree with the Institute of Remote Sensing and Geographic Information System, School of Earth and Space Sciences, Peking University, Beijing, China.

Her research interests include object detection and intelligent interpretation in visible and thermal infrared remote sensing images and videos.